Ceramics International 46 (2020) 24831–24837

Contents lists available at ScienceDirect

Ceramics International

journal homepage: www.elsevier.com/locate/ceramint

Cu_2O–ZnO heterojunction solar cell coupled to a $Ni(OH)_2$-rGO-PPy supercapacitor within a porous stoneware tile

J. Orozco-Messana[a,*], R. Daly[b], I.F. Zanchetta-Chittka[a]

[a] Instituto de Tecnología de Materiales, Universitat Politécnica de Valencia, Valencia, Spain
[b] Institute for Manufacturing, University of Cambridge, Cambridge, United Kingdom

ARTICLE INFO

Keywords:
BIPV
Supercapacitor
Heterojunction

ABSTRACT

Coupling photovoltaic solar energy (PV) generation with its storage for full availability is a key challenge for sustainable PVs. Tile integration of both can turn buildings or other urban structures, onto autonomous power units for low consumption electronics, sensors, and different e-services, through film printed electronics, ubiquitously available for future smart cities, support the deployment of the internet of things, and closing the gap to net zero energy buildings.

Starting from a porous stoneware tile, an electroless conductive Ni–Mo–P layer is the starting point for infiltrating on the connected porosity (3D free structure) of the tile thickness a nanostructured $Ni(OH)_2$-rGO-PPy composite acting as supercapacitor. On the open conductive surface an optimized p-Cu_2O/n-ZnO heterojunction was grown integrating a coupled charge-storage electrical circuit seamlessly on a commercial tile. The research presented on this paper has allowed the first experimental results of an autonomous, low-cost, energy supply system for future development of building integrated electronics.

1. Introduction

Future Smart Sustainable cities require low carbon energy procurement. Intermixed with this urban reality our society is demanding a viable solution for the rapid deployment of the Internet of things. Both realities require costly infrastructure development on old urban schemes [1].

The development of energy autonomous buildings thanks to renewable energies integrated onto building skins can reshape the dying ceramic sector in Europe. Functional ceramics can meet these requirements through a new concept: self-powered tiles [2]. These “smart” tiles should produce photovoltaic (PV) energy for its use and storage in a compact integrated unit. The novelty lies in fabricating efficient durable solar cells on the surface and embedding, within the open pore structure of the tile, a micro-capacitor (MIM) for industrial manufacturing of self-powering tiles by scalable low-cost processes.

When PVs, and sometimes MIMs, are concurrently developed making use of the building sun exposed surfaces (or building skin) they come into the category “Building Integrated Photovoltaic” (BIPV) systems. Such development is most efficient when both functionalities are integrated onto the architectural materials forming the building skin. BIPVs have attracted an increasing interest in the last few years [3] opening a very promising future for multifunctional ceramics.

Stoneware tiles are widely used on building skins offering important sun-exposed surfaces for photovoltaic energy generation. Their high resistance is required for architectural use and it is connected to low porosity.

Porcelain stoneware tile composition includes a combination of natural ceramic oxides such as SiO_2, Al_2O_3, TiO_2, ZrO_2, MnO, MgO, CaO, Na_2O and K_2O. Raw materials can be classified in three main groups by their composition and mineralogical structure and in relation to the specific function they perform: clays, silica minerals and feldspars. Several oxides appear in different crystalline phases which during firing are immersed in a vitreous matrix formed by the remaining components [4].

Clays have a definite illitic character (40–54%), a quartz content of approximately 30% and chlorite and kaolinite together comprising about 10%. The average content of hematite is around 5%. Potassic feldspar is more abundant than plagioclase although it never exceeds 7%. Through the firing process complex reactions take place which sometimes liberate gases easily evacuated before sintering takes place.

Sintered ceramics have a texture similar to rocks found on pyroclastic flows. Their microstructure can be classified (regarding composition) as rhyolitic–rhyodacitic according to Ref. [5]. Illite can be found up to at least 900 °C. From the destruction of illite an intermediate phase appears which slowly reacts at higher temperatures

* Corresponding author.
E-mail address: jaormes@cst.upv.es (J. Orozco-Messana).

https://doi.org/10.1016/j.ceramint.2020.06.229
Received 4 May 2020; Received in revised form 14 June 2020; Accepted 20 June 2020
Available online 08 August 2020

Table 1
Euroatomizado "Porcelanico estándar" chemical composition.

Oxide	SiO_2	Al_2O_3	CaO	MgO	Na_2O	K_2O	TiO_2	Fe_2O_3	Incineration loss 1000 °C
Weight %	59′85	15′99	4′87	3′59	1′45	1′30	0′61	0′48	11′9

eventually producing anorthite (from 1050 to 1100 °C). At higher temperatures mullite and other crystalline phases are formed as well as an abundant vitreous phase. Microcrystalline growth occurs at the expense of the vitreous matrix as can be seen on the internal face of pores. As temperature grows during sintering the vitreous phase is decanted from a microcrystalline mass pores connection first, and then isolated pores.

However, controlled connected porosity in their thickness allow an exponential growth of the surface available for energy storage which can be used for energy storage integration. During firing phyllosilicates and accompanying minerals, undergo different phase changes controlling the final tile properties. These phases partially decompose during the ceramic process leaving connected pores which are later filled in by vitreous components at high temperatures. An internal (connected) porosity up to 20% can maintain the required bending strength [6] while opening an interconnected internal surface of 75 m^2 per square meter tile.

For the electrical functionalization of ceramics there are few techniques allowing conductive surface preparation. These layers are especially complex over ceramics due to the coating adherence and surface topology. Most deposition techniques are not valid for unglazed ceramics (thin films) and must be tuned for adequate adherence. Among the few feasible techniques [7] electroless deposition appears as the most adequate option.

The key requirement is efficient (average daily conversion), durable power generation performance with low-cost, bearing also in mind esthetic impact on facades. According to the latest solar-cell ranking published by Green et al. [8] the first candidates should be considered among the homojunction, or multi-junction solar cell types. However, the production costs and requirements [9] rule out their use on the envisaged application due to the impossibility to integrate (physically) these cells on a tile.

The second-best alternative is heterojunction cells. Different families, either Perovskites [10] or organic based cells [11] show good energy performance but very constrained in their durability (and technical requirements). A very promising family is metal oxide heterojunction cells [12] which although limited on top efficiency, show the best compromise for maintained solar energy harvesting.

BIPV requires for its full development the capability of storing energy in flexible, efficient and long-lasting systems. Due to the non-predictable availability of solar energy completely autonomous systems have not been possible or require more expensive alternatives than switchable energy supplies.

Energy storage becomes the second most relevant constraint for an effective success of BIPVs. There are many competing energy storage technologies with technical proficiency that can be commercial alternatives on this role [13]. The most mature systems are difficult to integrate, while better tuned alternatives are expensive solutions with their current industrial formats.

A comprehensive review of current energy storage alternatives has been presented and analyzed in Ref. [14]. Comparing their storage principle, functionalities, availability, maintenance requirements and balanced dimensioning, very few can be considered for BIPV integration. Only Compressed Air Energy Storage (CAES), several types of batteries, Hydrogen Fuel Cells, Phase Change Materials (PCM), and Supercapacitors are real alternatives. However, the most critical parameters are investment and operational costs, together with power and energy densities. These narrow down the optimal selection to the new carbon-based supercapacitors.

Recent developments on reduced Graphene Oxide (rGO) based electrodes for supercapacitors show properties matching the already presented requirements [15]. Electrode design and fabrication make all the difference on this critical application. The correct performance of these devices when integrated on architectural materials, depend on the correct design of their nano structured surface morphology for the electrode. Besides durability demands an all solid-state hybrid supercapacitor using coupled nanostructures for both cathode and anode.

This paper presents the first integration of both solar generation from a Cu_2O/ZnO heterojunction PV cell and storage with a rGO supercapacitor-based onto a commercial ceramic tile with satisfactory results for their use on BIPV functionalities.

2. Material and methods

2.1. Ceramic substrate

For preparing the porcelain stoneware substrate the atomized ceramic powder used was provided by the Euroatomizado group. The formulation selected corresponds to their standard "gres porcelanico" which is a typical representative of commercial porcelain stoneware ceramic tiles at industrial level. On Table 1 the chemical composition of the powder is presented with the different oxides present.

Rectangular samples were dry pressed on a steel die following the prescribed specific pressure of 380 kg/cm^2 obtaining an apparent density of 2′08 gr/cm^3. On the green state after pressing samples were 50 × 15 mm with a thickness of 5 mm. Firing was performed on an electric kiln following a ramp of 20 °C/min up to 1.100 °C.

2.2. Electroless optimized Ni–Mo–P conductive layer

As indicated on the introduction, the conductive layer of choice was obtained by electroless deposition. Within the range of possible layers Ni–Mo–P shows the most attractive profile, not only due to its electrical properties (conductivity and energy level alignment) but also it is a low-cost, easily applied and scalable process allowing the deposition of homogeneous alloy coatings with uniform thickness on a non-conductive surface. An additional incentive is the catalytic texture which can be produced with Ni through its hydroxide, $Ni(OH)_2$, for developing a composite with rGO for a nanostructured binder-free conductive electrode for supercapacitors [16].

The optimization of the Ni–Mo–P electroless deposition process has been studied by our research group [17] and can be summarized as follows:

- After cleaning, rinsing and drying the fired ceramic substrates, the activation process is performed spraying a Pd catalyst ink. The ink formulation was prepared as follows: Solution (A) containing 1 gr of Butvar solved in 50 ml of 1-propanol continuously stirred for 2 h. Solution (B) consisting of 0′19 gr of palladium acetate in 0′5 ml of ammonium hydroxide which was added to the solution (A) to form the Pd catalyst ink. The catalyst sprayed ceramic is put on an electric kiln at 400 °C for 12 h for activation.
- The activated samples were immersed in the Ni–Mo–P plating bath. The bath consisted of 7′0 gr/l of $NiSO_4$ and 3′9 gr/l of Na_2MoO_4 as metallic precursor, and 10 gr/l NaH_2PO_2 as reducing agent, 10′0 gr/l $C_6H_{12}O_7$ and 15 gr/l of $Na_2C_4H_4O_6$ as stabilizing agents and NH_4OH as complexing agent and pH adjuster. The electroless deposition was performed at pH 10, 80 °C, for 30 min with constant

stirring at 300 rpm. Finally, substrates were rinsed with water to finish the reaction and air dried.
- An additional heat treatment of the samples at 400 °C for 12 h reduces the resistivity and the surface roughness.

2.3. Supercapacitor $Ni(OH)_2$-rGO-PPy

Both low resistivity and high specific surface area are the objectives pursued on a high-performance supercapacitor. In our application the Ni–Mo–P layer must be reduced to $Ni(OH)_2$ for later adding rGO to its nanostructure. As shown on [16] this enables the storage of relevant amounts of charge through its faradaic reaction, which is enhanced by the excellent conductivity of the rGO grown on the nanostructure of Ni $(OH)_2$ [18] on the back of the Ni–Mo–P layer.

Accordingly the back of the Ni–Mo–P electroless layer has to be reduced to develop a nanostructured 3D foam of $Ni(OH)_2$ [16]. This is done chemically by putting the porous ceramic sample on a solution 0′1 M $Ni(NO_3)_2{\cdot}6H_2O$ solution and 0′2 M in urea. After putting the solution under continuous magnetic stirring for 10 min, the ceramic sample is put on top without the liquid touching the metallic surface. After 10 min at room temperature the solution is adsorbed by the ceramic porous structure. The back of the Ni–Mo–P layer develops a foam of $Ni(OH)_2$ on the interface and is connected to the porous micro structure. Later samples are dried at 60 °C for 2 h in a closed oven.

A separate 1 mg/ml GO solution was prepared from a Sigma-Aldrich 2 mg/ml, dispersion in H_2O. After the dilution process in deionized water during 30 min through an ultrasonication process the solution is adsorbed in the open porous structure of the ceramic sample as before. After 1 h samples are dried again as indicated before. The last process is the reduction of the adsorbed GO which is done through cyclic voltammetry (0′01 to -1′4 Vdc, 5 cycles) in a 0′1 M KCl solution with a sweep speed of 50 mV/s. Standard drying follows.

These electrodes work well as supercapacitors but, cycling instability appears quickly. In order to enhance the service life (which is critical for this application) several authors [19] used PPy nano-leaves serving as backbone and conductive shortened conductive paths among $Ni(OH)_2$ nano leaves. When the pyrroles polymerize among the Ni $(OH)_2$ enhanced cyclic stability is obtained. To obtain polypyrrole (PPy) the reagents (from Sigma-Aldrich) used were: sodium 0′02 M p-toluenesulfonate (NapTS), 5% volume solution of pyrrole monomer (Py) and 0′02 M sodium dodecylsulfate.

The cyclic voltammetry was performed using an Autolab PGSTAT302 N potentiostat. The solution is used for a 30 cycle cyclic voltammetry electrodeposition from -0′01 to 1′00 V (sweep speed 30 mV/s) which produces the polymerization of the pyrrole monomers (PPY). Standard drying follows.

The last step for finishing the supercapacitor includes closing empty spaces as much as possible with a stable electrolyte with good conductivity. The preparation of Polyvinyl alcohol (PVA)-KOH-H_2O alkaline gel polymer electrolyte serves the purpose and can be adsorbed and remains in place after adsorption. The mass ratio used was m(PVA):m (KOH) is 3:4.5 [16]. Reagents used were from Panreac and 20 gr of the solid is solved in 30 ml deionized water. Once again, the solution is adsorbed in the ceramic internal structure for 3 h for later drying at 100 °C for 1 h. The supercapacitor is sealed by a carbon-fibre textile attached to the back of the ceramic serving also as back contact.

2.4. Cu_2O/ZnO heterojunction PV cell

The research for the development and optimization of the Cu_2O/ZnO heterojunction PV cell was already reported by our research team in Ref. [20]. For this application the reagents used were bought from Panreac and used as received:

- For the electrodeposition of ZnO, a 5 mM solution of zinc chloride ($ZnCl_2$) and 0′1 M of potassium chloride (KCl), controlling pH to 6, is used. The equipment used was an Autolab PGSTAT302 N.
- For the electrodeposition of Cu_2O the electrolytic solution was 0′4 M in copper (II) sulfate pentahydrate ($CuSO_4{\cdot}5H_2O$, 85%), 3 M in lactic acid ($C_3H_6O_3$, 85%) and 4 M in sodium hydroxide (NaOH).

The ZnO layers were synthesized over the free surface of the Ni–Mo–P layer previously obtained. The process was potentiostatic electrodeposition using a conventional three-electrode cell. Metallized ceramic substrates were used as working electrodes, a platinum wire as the counter electrode and an Ag/AgCl electrode in a saturated solution of KCl as a reference electrode. A 5 mM $ZnCl_2$ and 0.1 M KCl solution was prepared, saturated with oxygen by continuous bubbling. The electrodeposition process was carried out at a potential of −0.8 V for 30 min at a temperature of 75 °C, which was maintained throughout the process within a water bath. The pH of the solution was 6. At the end of the process, the metallized ceramic substrates modified with a layer of ZnO were obtained.

Once the ZnO layer was electrodeposited on the metallic ceramic substrate, the Cu_2O layer was electrodeposited to obtain a p-n heterojunction type solar cell. The Cu_2O layer was synthesized using a conventional three-electrode cell, where the previous ZnO layer over the ceramic was used as working electrode, a platinum wire as a counter electrode and an Ag/AgCl as reference electrode. The electrodeposition process was carried out at a constant potential of −0.6 V at a temperature of 35 °C, using a water bath, for 5 h. Upon completion, the substrates were rinsed with distilled water and air dried.

3. Ceramic assembly design

The devices introduced in the previous point have been selected and designed for a parallel connection of the solar cell to the supercapacitor. The optimal operation of each Cu_2O/ZnO cell is around 230 mV [20]. Thus, the asymmetric supercapacitor device is operating within the possible potential range available (from 0′1 to 0′7 V) as will be presented on the next point. This assembly will be evaluated also in the results section. The block diagram of the integrated tile is shown on Fig. 1.

4. Results

4.1. Ceramic substrate

After firing the properties of the ceramic substrates were measured. Porosity was evaluated with a Bruker SKYSCAN 1272. The tomographic c-scans were performed at CT scanning was ran at 140 kV and 10 W. Later computer calculations estimated the open porosity between 15 and 20% with a final bending strength was 42–48 N/mm^2.

The equipment used for imaging was Zeiss Ultra55 FESEM. Surface texture and open porosity are presented on Fig. 2.

4.2. Electroless optimized Ni–Mo–P conductive layer

Fig. 3 shows the AFM and FESEM images of the modified ceramic substrates with a Ni–Mo–P layer. The Ni–Mo–P optimal coating obtained presents a thickness of approximately 465 ± 22 nm (from FIB cross section). For fibbing the equipment used was a Zeiss Auriga Compact FESEM equipped with FIB.

The resistivity was measured with an Ecopia Hall-effect equipment and evaluated in 10′6 ± 2′2 μΩ cm. As proof of the adhesion quality for the metallic layer a PosiTest AT-100 equipment was used with a value of 7′2 ± MPa.

4.3. Supercapacitor $Ni(OH)_2$-rGO-PPy

Fig. 4 shows the morphologies for the back of the ceramic substrates after the different deposition processes. As can be seen in Fig. 4b and c

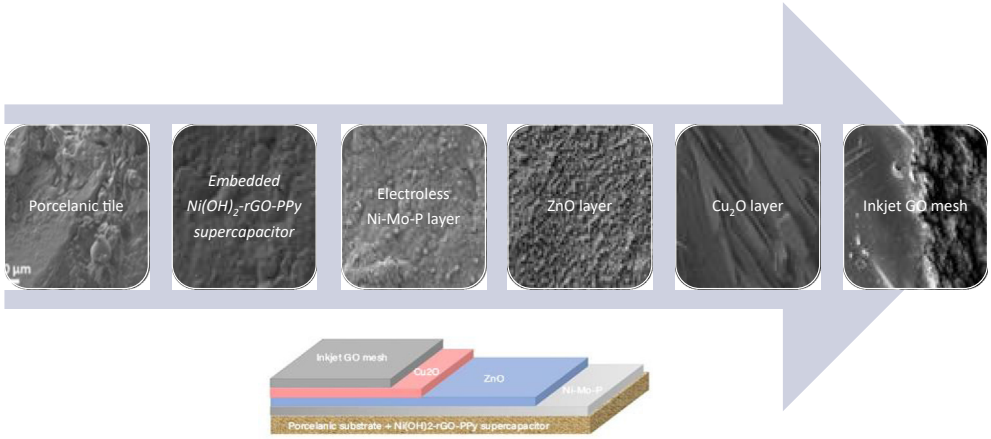

Fig. 1. Sample assembly block diagram.

there is a slight difference with Fig. 4a, in these images it is possible to see the presence of a thin and dark layer on the surface of the ceramic substrate, which slightly changes the morphology of the surface may be due to the presence of Ni(OH)2-rGO layers. Only slight texture changes can be seen when the PPy layer is added.

Fig. 5 shows the Current/Voltage (CV) curves of the Ni–Mo–P ceramic substrate alone and the hybrid $Ni(OH)_2$-rGO-PPy electrode at scan rates of 2, 10, 25, 50 and 100 mV/s. When comparing the CV curves, the enhanced performance in the electrochemical behavior of the $Ni(OH)_2$-rGO-PPy electrode, thus demonstrating the synergistic effect of its $Ni(OH)_2$-rGO elements., which provides EDLC features; and PPy, which gives the pseudo condenser behavior. The areal capacitance at 2 mV/s of the ceramic substrate is equal to 1′05 mF/cm^2, while that of the PPy/rGO hybrid electrode is 32′77 mF/cm^2. With this, it is possible to modify the surface morphology, as can be seen in Fig. 3, and considerably increase its conductivity, thus improving its areal capacitive performance.

As can be seen in Fig. 6a, the $Ni(OH)_2$-rGO-PPy hybrid electrode shows an oxide-reduction peak in its voltammograms around + 0.6 V. In addition, it is observed that the capacitive performance increases with passing from 1 to 500 cycles, as the AC values were equal to 12′56 and 16′45 mF/cm^2, respectively. According to what is shown in Fig. 6b there is a significant increase in the AC of the $Ni(OH)_2$-rGO-PPy hybrid electrode as a function of the number of cycles. It can be seen that the highest point occurs at 200 cycles, where the AC value is 16/68 mF/cm^2, then a slight decrease occurs at 16′35 mF/cm^2 (400 cycles) and it is possible that the electrode stabilizes (500 cycles). Given the fact that the AC in this type of hybrid electrode increases, instead of decreasing as the number of cycles increases, it can be said that it is an electrode with a long-term cyclability.

4.4. Cu_2O/ZnO heterojunction PV cell

The crystal structure of the ZnO and Cu_2O electrodeposited layers was determined by means of an X-ray diffraction characterization. The diffraction spectra of the heterojunction Cu_2O/ZnO junction electrodeposited under different conditions is shown in Fig. 7.

The diffraction patterns confirmed the existence of polycrystalline ZnO layers with a wurtzite-like hexagonal crystal structure and a preferential orientation in the plane (101). Furthermore, the peak (100) of ZnO was identified, according to identification letter JCPDS 00-036-1451. Regarding the synthesized Cu_2O layers, it can be said that these showed a strong intensity in the peak (111), which indicates the preferential orientation of potentiostatic electrodeposition of Cu_2O.

The morphology and thickness evaluation of the electrodeposited ZnO and Cu_2O layers were analyzed by FE-SEM microscopy with FIB. Fig. 8 represents a typical cross section of the n–p junction of Cu_2O/ZnO and their corresponding thickness values: 543 nm for ZnO and 8.220 nm for Cu_2O layers, obtained by FIB.

Once the manufacturing process of the p–n junction type solar cells was completed, the photoelectric characterization of the Cu_2O/ZnO sample solar cells was done using the Autolab PGSTAT302 N potentiostat connected to a calibrated solar simulator AM1.5G with a radiation intensity of 100 mW/cm^2 at 25 °C. The average values of the photoelectric parameters obtained were short-circuit current density (J_{SC}) 317 μA/cm^2, and open circuit voltage (V_{OC}) 240 mV.

Once the heterojunction Cu_2O/ZnO was characterized the remaining task is to prepare the front contact and both solar

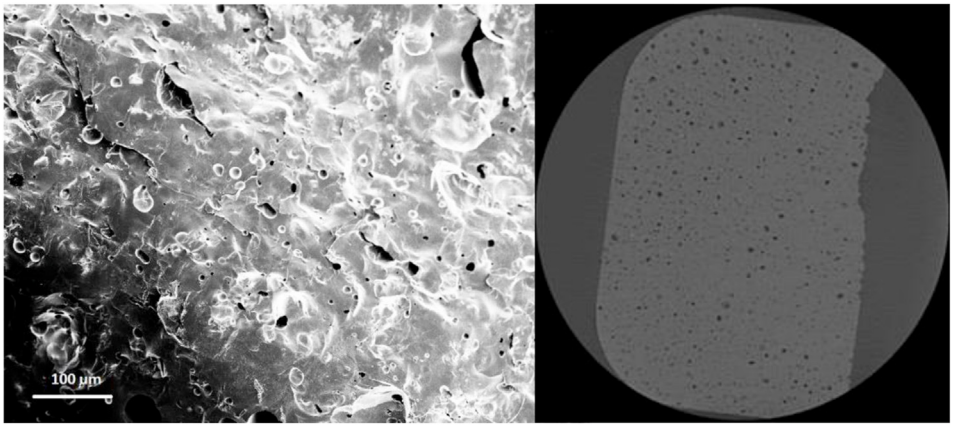

Fig. 2. Sample surface and porosity CT-scan check for a 1.100 °C fired sample.

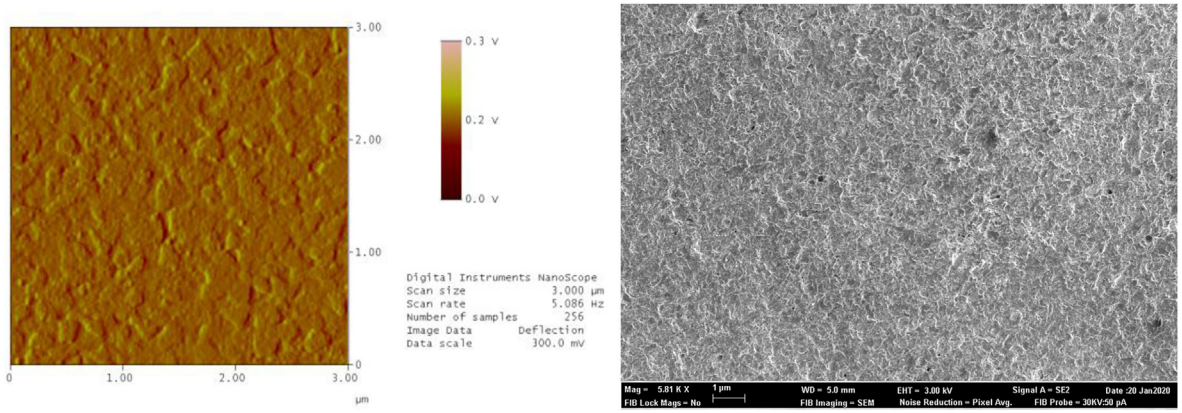

Fig. 3. Surface texture of the Ni–Mo–P layer seen through AFM and FESEM.

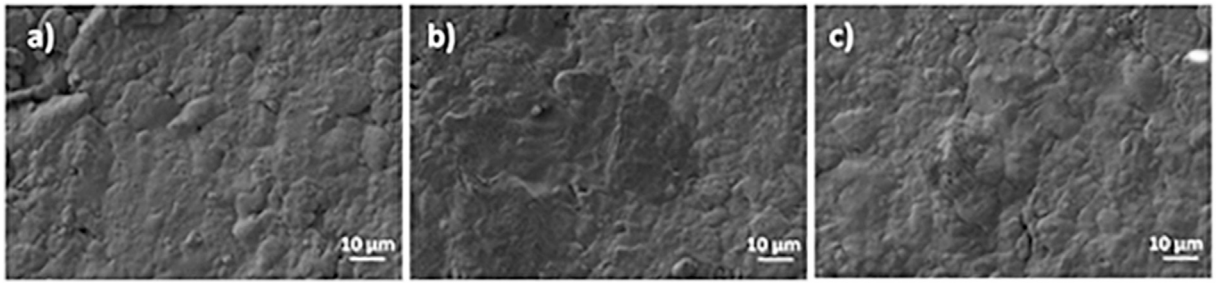

Fig. 4. FE-SEM texture: (a) ceramic substrate; (b) Ni(OH)2-rGO; (c) $Ni(OH)_2$-rGO-PPy.

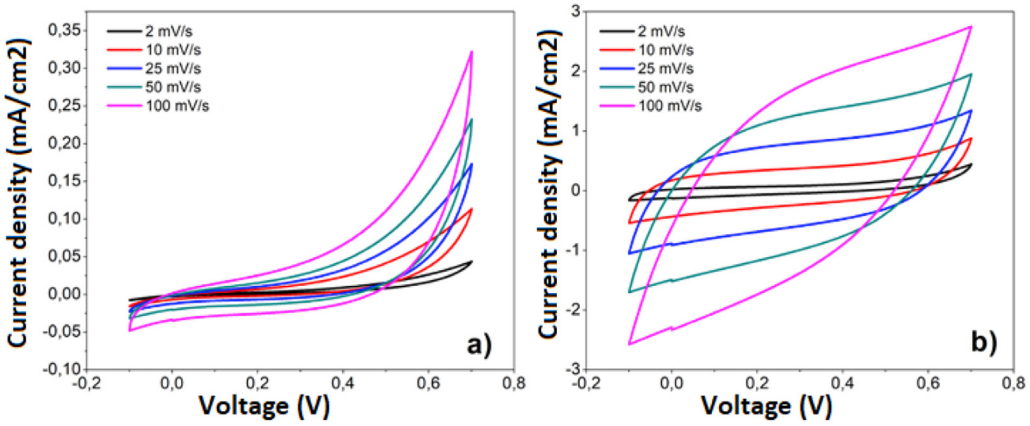

Fig. 5. CV curves (2–100 mV/s sweeps) for: a) Ni–Mo–P/rGO; b) $Ni(OH)_2$-rGO-PPy.

heterojunction and supercapacitor will be in parallel between the front contact and the back carbon-fiber textile sealing. The front contact then must be transparent covering well the surface without interference with the sun light.

The solution was to inkjet print a square mesh of graphene oxide (GO) tiny paths on the surface. Based on previous tests performed with different inks at the Institute for Manufacturing (University of Cambridge) it was decided to use a GO inkjet using water as solvent. First, 50 ml of a graphene oxide dispersion with a concentration of 2 mg/ml was bought from Sigma-Aldrich. Second, 10 ml dimethyl carbinol (from Spectrum Chemical) and 0′6 g Dynol 465 (from Evonik) were added to the dispersion and stirred for 12 h to obtain a uniformly dispersed solution. Third, using inkjet printer Domino G20i thermal inkjet printer, and print head with a nozzle diameter of 40 µm to print graphene oxide lines on the surface of the Cu_2O/ZnO heterojunction with a substrate temperature of 50 ˚C. Each line was 50 µm wide after printing and each line was separated 10 mm from any other.

5. Discussion

The ceramic samples used are representative of commercial architectural tiles for building envelopes. They have been adjusted to couple to integrated functionalities which are using the tile's microstructure and devices integration in a synergetic way without losing their original purpose.

A metallic Ni–Mo–P coating has been obtained using the electroless method on a ceramic substrate. The balance of properties through optimized catalyst activation condition of 300 ˚C for 12 h. The coating presented a stable crystalline structure with a typical nodular morphology which allowed the synergetic coupling of a supercapacitor by reducing the back surface to flakes of $Ni(OH)_2$.

The tailored design of the supercapacitor has been successfully adapted to the connected porosity network including rGO and PPy as enhancing elements for balancing photovoltaic energy storage from the Cu_2O/ZnO heterojunction. The capacitance properties of the hybrid

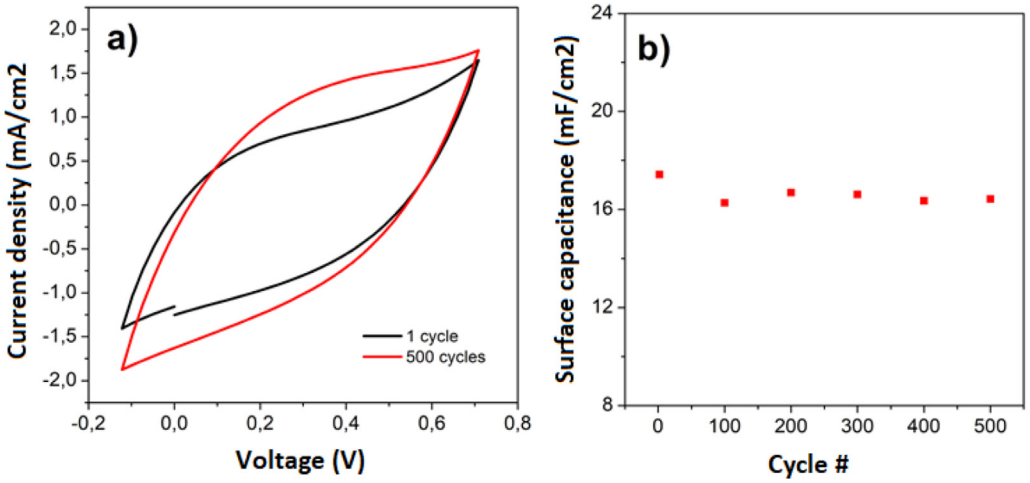

Fig. 6. $Ni(OH)_2$-rGO-PPy (a) CV curve at 50 mV/s; (b) Area capacitance with cycle #.

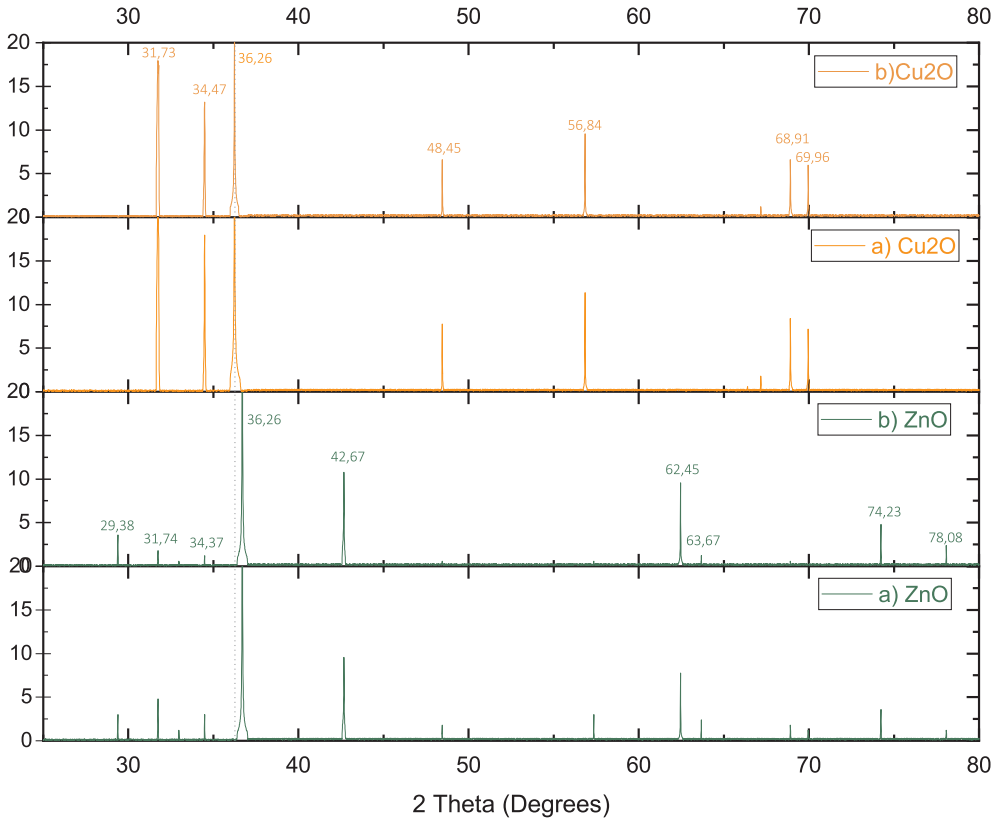

Fig. 7. X-ray diffraction spectra in perpendicular directions (a,b) ZnO, (c,d) Cu_2O.

electrode were observed to increase with the active material loading, namely rGO and PPy. The solar cell is lacking further development to obtain a valid commercial efficiency. More room for improvement exists for advancing towards a really transparent PV material which would improve the successful commercial deployment of these "smart" tiles.

Building front contacts with inkjet printed rGO is a promising alternative which requires an optimization. The technique has been proved as feasible but has many gaps to fill in for durable and efficient performance.

6. Conclusions

This paper has demonstrated the potential use of ceramic substrates for the simultaneous generation and storage of photovoltaic energy.

Starting from a non-standard preparation of the porcelanic tile, generated porosity allowed the integration on the connected pore internal surface of an asymmetric supercapacitor device $Ni(OH)_2$/rGO/PPy. This supercapacitor presents an excellent energy density of 26′3 Wh/kg and power density of 2.918 kW/kg.

On the external surface an electroless Ni–Mo–P metallic coating was optimized to work as the back contact of a electrodeposited solar cell. The assembled supercapacitor is therefore coupled to a low cost Cu_2O/ZnO heterojunction solar cell which has been tested to generate power with a reasonable efficiency.

The greatest achievement however, has been the fabrication of a self-sustainable autonomous unit integrated on a commercial façade tile. When scaled to a full building envelop this can contribute to real

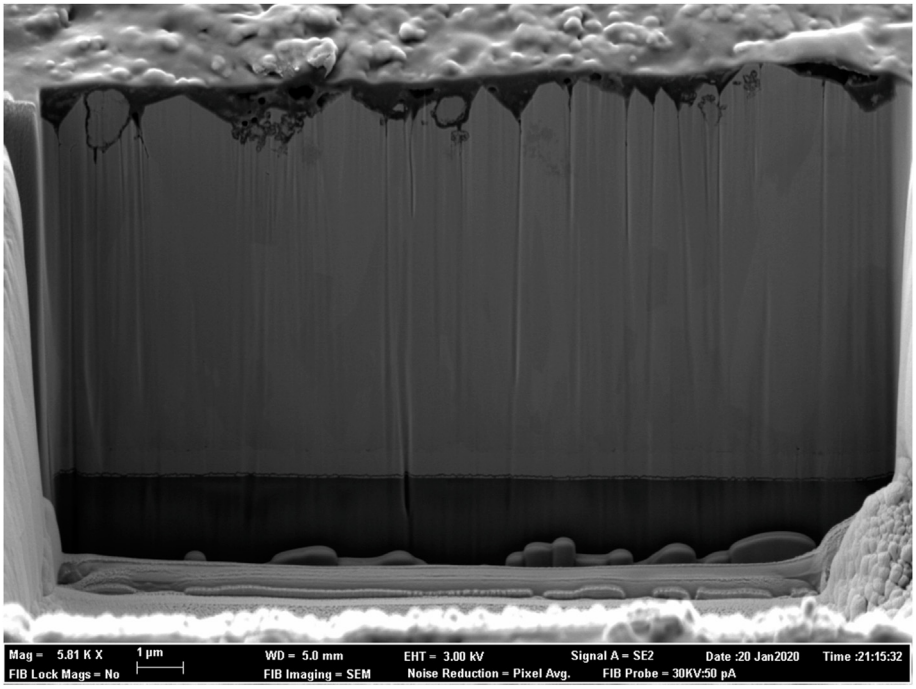

Fig. 8. Transversal section of the p-n junction p–n de Cu_2O/ZnO.

nZEBs [21].

Declaration of competing interest

The authors declare that they have no known competing financial interests or personal relationships that could have appeared to influence the work reported in this paper.

Acknowledgements

The authors would like to acknowledge the support from the Institute for Manufacturing at the University of Cambridge for supporting the initial work of inkjet developments.

Appendix A. Supplementary data

Supplementary data related to this article can be found at https://doi.org/10.1016/j.ceramint.2020.06.229.

References

[1] D. Sarkar, A. Shukla, A. Kumar, P.K. Sadhu, Role of internet of things (IoT) in maximum power extraction from BIPV modules: a review for developing smart zero energy buildings, Int. J. Eng. Technol. 7 (3.12) (2018) 1033–1037.
[2] G. Gokul, S.C. Pradhan, S. Soman, Dye-sensitized solar cells as potential candidate for indoor/diffused light harvesting applications: from BIPV to self-powered IoTs, Advances in Solar Energy Research. Energy, Environment, and Sustainability, Springer, Singapore, 2019, https://doi.org/10.1007/978-981-13-3302-6_9.
[3] A.K. Shukla, K. Sudhakar, P. Baredar, Recent advancement in BIPV product technologies: a review, Energy Build. 140 (2017) 188–195, https://doi.org/10.1016/j.enbuild.2017.02.015.
[4] N.T. Selli, Development of anorthite based white porcelain stoneware tile compositions, Ceram. Int. 41 (6) (2015) 7790–7795, https://doi.org/10.1016/j.ceramint.2015.02.112.
[5] M. Raimondo, C. Zanelli, G. Guarini, M. Dondi, R. Fabbroni, T. Cortesi, Process of pyroplastic shaping for special-purpose porcelain stoneware tiles, Ceram. Int. 35 (5) (2009) 1975–1984, https://doi.org/10.1016/j.ceramint.2008.10.017.
[6] V. Cannillo, L. Esposito, E. Rambaldi, A. Sola, A. Tucci, Effect of porosity on the elastic properties of porcelainized stoneware tiles by a multi-layered model, Ceram. Int. 35 (1) (2009), https://doi.org/10.1016/j.ceramint.2007.10.015 205-21.
[7] R. He, G. Schierning, K. Nielsch, Thermoelectric devices: a review of devices, architectures, and contact optimization, Adv. Mater. Technol. 3 (2018), https://doi.org/10.1002/admt.201700256.
[8] M.A. Green, E.D. Dean, H.L.J. Hohl-Ebinger, M.Y. Anita, W.Y. Ho-Baillie, Solar cell efficiency tables (version 54), Prog. Photovoltaics 27 (7) (2019) 565–575, https://doi.org/10.1002/pip.3171.
[9] N. Ali, R. Ahmed, J.T. Luo, M. Wang, A. Kalam, A.G. Al-Sehemi, Y.Q. Fu, Advances in nanostructured homojunction solar cells and photovoltaic materials, Mater. Sci. Semicond. Process. 107 (2020) 104810, , https://doi.org/10.1016/j.mssp.2019.104810.
[10] M. Kim, S.G. Motti, R. Sorrentino, A. Petrozza, Enhanced solar cell stability by hygroscopic polymer passivation of metal halide perovskite thin film, Energy Environ. Sci. 11 (2018) 2609–2619, https://doi.org/10.1039/C8EE01101J.
[11] W. Huang, Z. Jiang, K. Fukuda, X. Jiao, C.R. McNeill, T. Yokota, T. Someya, Efficient and mechanically robust ultraflexible organic solar cells based on mixed acceptors, Joule 4 (1) (2020) 128–141, https://doi.org/10.1016/j.joule.2019.10.007.
[12] M.G. Kohan, I. Concina, A. Vomiero, Chapter Six - All-Oxide Solar Cells, Solar Cells and Light Management, Elsevier, 2020, pp. 229–246, https://doi.org/10.1016/B978-0-08-102762-2.00006-9.
[13] M.C. Argyrou, P. Christodoulides, S.A. Kalogirou, Energy storage for electricity generation and related processes: technologies appraisal and grid scale applications, Renew. Sustain. Energy Rev. 94 (2018) 804–821, https://doi.org/10.1016/j.rser.2018.06.044.
[14] C. Lamnatou, G. Notton, D. Chemisana, C. Cristofari, Storage systems for building-integrated photovoltaic (BIPV) and building-integrated photovoltaic/thermal (BIPVT) installations: environmental profile and other aspects, Sci. Total Environ. 699 (2020) 134269, , https://doi.org/10.1016/j.scitotenv.2019.134269.
[15] S. Karthik Kiran, S. Shukla, A. Struck, S. Saxena, Surface enhanced 3D rGO hybrids and porous rGO nano-networks as high performance supercapacitor electrodes for integrated energy storage devices, Carbon 158 (2020) 527–535, https://doi.org/10.1016/j.carbon.2019.11.021.
[16] P.E. Lokhande, U.S. Chavan, Nanostructured $Ni(OH)_2$/rGO composite chemically deposited on Ni foam for high performance of supercapacitor applications, Mater. Sci. Energy Technol. 2 (1) (2019) 52–56, https://doi.org/10.1016/j.mset.2018.10.003.
[17] N.M. Rosas-Laverde, A. Pruna, J. Cembrero, M. Pascual, J. Orozco-Messana, Optimizing electroless plating of Ni–Mo–P coatings toward functional ceramics, Acta Metall. Sin. 33 (2020) 437–445, https://doi.org/10.1007/s40195-019-00989-x.
[18] S. Aslam, F. Mustafa, M.A. Ahmad, Facile synthesis of graphene oxide with significant enhanced properties for optoelectronic and energy devices, Ceram. Int. 44 (6) (2018) 6823–6828, https://doi.org/10.1016/j.ceramint.2018.01.105.
[19] X. Li, J. Wang, One-dimensional and two-dimensional synergized nanostructures for high-performing energy storage and conversion, InfoMat 2 (1) (2020) 3–32, https://doi.org/10.1002/inf2.12040.
[20] N.M. Rosas-Laverde, A. Pruna, D. Busquets-Mataix, B. Marí, J. Cembrero, F. Salas Vicente, J. Orozco-Messana, Improving the properties of Cu2O/ZnO heterojunction for photovoltaic application by graphene oxide, Ceram. Int. 44 (18) (2018) 23045–23051, https://doi.org/10.1016/j.ceramint.2018.09.107.
[21] R.A. Agathokleous, S.A. Kalogirou, Status, barriers and perspectives of building integrated photovoltaic systems, Energy 191 (2020) 116471, , https://doi.org/10.1016/j.energy.2019.116471.